

# CHROMA: CONSISTENT HARMONIZATION OF MULTI-VIEW APPEARANCE VIA BILATERAL GRID PREDICTION

Jisu Shin\*

Huawei Noah’s Ark Lab  
GIST AI Graduate School

Richard Shaw

Huawei Noah’s Ark Lab

Seunghyun Shin

GIST AI Graduate School

Zhensong Zhang

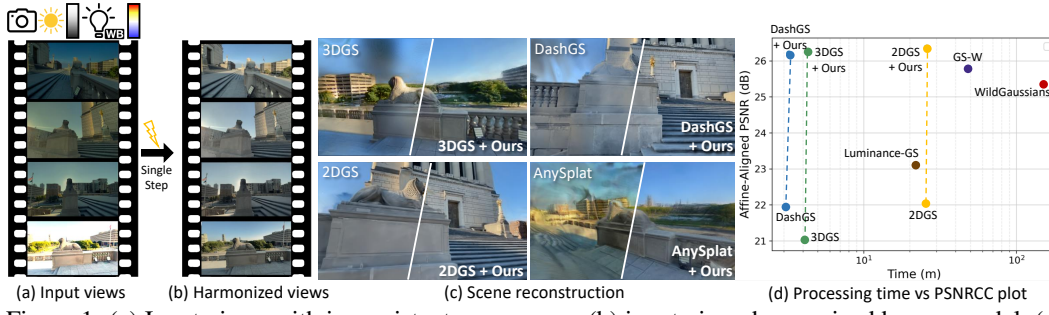
Huawei Noah’s Ark Lab

Hae-Gon Jeon†

Yonsei University

Eduardo Pérez-Pellitero†

Huawei Noah’s Ark Lab



## ABSTRACT

Modern camera pipelines apply extensive on-device processing, such as exposure adjustment, white balance, and color correction, which, while beneficial individually, often introduce photometric inconsistencies across views. These appearance variations violate multi-view consistency and degrade novel view synthesis. Joint optimization of scene-specific representations and per-image appearance embeddings has been proposed to address this issue, but with increased computational complexity and slower training. In this work, we propose a generalizable, feed-forward approach that predicts spatially adaptive bilateral grids to correct photometric variations in a multi-view consistent manner. Our model processes hundreds of frames in a single step, enabling efficient large-scale harmonization, and seamlessly integrates into downstream 3D reconstruction models, providing cross-scene generalization without requiring scene-specific retraining. To overcome the lack of paired data, we employ a hybrid self-supervised rendering loss leveraging 3D foundation models, improving generalization to real-world variations. Extensive experiments show that our approach outperforms or matches the reconstruction quality of existing scene-specific optimization methods with appearance modeling, without significantly affecting the training time of baseline 3D models.

## 1 INTRODUCTION

Novel view synthesis (NVS) and 3D reconstruction are fundamental challenges in computer vision and graphics. Recent advances, such as Neural Radiance Fields (NeRF) (Mildenhall et al., 2020) and 3D Gaussian Splatting (3DGS) (Kerbl et al., 2023), have significantly improved the fidelity and

\*Work done during an internship at Huawei Noah’s Ark Lab, UK

†Corresponding Authors

---

realism of scene reconstruction and rendering. These methods typically rely on multi-view images captured under the assumption of photometric consistency across views. However, this assumption often breaks in real-world scenarios due to various sources of photometric inconsistency, including: (i) in-camera Image Signal Processing (ISP) variations, e.g. exposure, white balance, color correction; and (ii) scene illumination. Such inconsistencies degrade reconstruction quality, producing floaters, color artifacts, or generally unstable results. To address these challenges, prior art has explored per-view appearance embeddings (Martin-Brualla et al., 2021; Kulhanek et al., 2024; Wang et al., 2024a; Xiao et al., 2025; Cui et al., 2025), providing reconstruction with additional capacity to capture per-view appearance variations via MLPs, tone curves, or affine transforms that are jointly learned with the scene in a global multi-view optimization. While effective, these approaches tightly couple appearance modeling with geometry reconstruction, incurring additional computation at each optimization step, substantially increasing training cost. This undermines the efficiency of pipelines designed for speed, e.g. 3DGS and recent extensions (Mallick et al., 2024; Chen et al., 2025) which achieve rapid scene fitting. Moreover, the recovered appearance after removing the embeddings is not explicitly controllable and often converges to the mean of all variations observed in the input views.

These limitations motivate decoupling appearance harmonization from scene optimization and addressing it in a feed-forward manner, promising improvements in accuracy, controllability, and efficiency. However, several challenges remain when treating this as an independent problem. Existing 2D image and video enhancement techniques (Afifi et al., 2021; Cui et al., 2024; Li et al., 2024; Zhou et al., 2024; Cui et al., 2022; Shin et al., 2023; 2024a) often lack temporal or multi-view consistency, address only limited types of appearance variation (e.g. exposure correction), and struggle to robustly handle severe color shifts or saturation artifacts. Additionally, most approaches require fully-supervised learning paradigms, yet collecting paired real-world data is infeasible: real-world appearance variations are inherently unique in time and space, and one cannot easily capture pixel-aligned images where several appearance variations can be isolated and used as labels.

In this work, we address the aforementioned challenges by introducing a feed-forward approach to multi-view appearance harmonization tailored for 3D reconstruction from varying appearance images. Given multi-view captures of a static scene and a reference frame with a desired appearance, our model transforms all views to match the reference, ensuring photometric consistency. Our key idea is to learn per-frame 3D bilateral grids of affine transforms in a generalizable, multi-view consistent manner. We use bilateral grids as they are compact and expressive, capable of modeling a wide range of ISP operations (Chen et al., 2007; Gharbi et al., 2017; Shin et al., 2024b) and beyond. A multi-view aware transformer predicts low-resolution bilateral grids for each view, which, when applied to the inputs, aligns their appearance with the reference at full resolution. To make the model uncertainty-aware, we also predict bilateral confidence grids using a probabilistic loss. We introduce a reference selection strategy that identifies the image most representative of overall scene appearance, avoiding outliers that could degrade reconstruction quality. Selection is driven by a weighted ranking score accounting for both intensity and semantic similarity, ensuring the final appearance is realistic (i.e. not an average over all frames), while providing flexibility for either manual choice or automatic selection. Lastly, we address the lack of training data for such a system by proposing (i) a synthetic data-generation pipeline to handle large granularity image-level variations, and (ii) a self-supervised training paradigm that uses recent large 3D reconstruction models as a pretext task to provide real-data training signals.

Unlike prior art, our lightweight transformer model introduces only a fixed computational cost per frame. This decoupled design allows seamless integration into pipelines such as 3DGS (Kerbl et al., 2023), 2DGS (Huang et al., 2024a), DashGS (Chen et al., 2025), and even feed-forward models (Jiang et al., 2025), enhancing view consistency while preserving scalability and speed. Through our hybrid self-supervised and supervised (synthetic data) approach, our model achieves state-of-the-art accuracy for real-world datasets, which in turn also improves the robustness and stability of 3DGS optimization under challenging photometric conditions without negatively affecting training time. Comprehensive evaluation demonstrates that our model matches and often exceeds the performance of existing 3DGS-based appearance embedding approaches while maintaining competitive training speed.

---

## 2 RELATED WORKS

**Appearance Correction and Bilateral Grids.** Image correction aims to adjust visual attributes such as exposure, white balance, and tone to improve image quality or ensure consistency. Traditional methods solve this using histogram equalization (Zuiderveld, 1994), retinex-based methods, or global transformation optimization, but often lack spatial adaptability. Learning-based approaches (Afifi et al., 2021; Afifi & Brown, 2020; Zhou et al., 2024) address these issues using CNNs, but struggle with generalization or fine detail preservation. Bilateral filtering has been widely used due to its edge-aware properties. Numerous approaches improve its efficiency, such as convolution pyramids (Farbman et al., 2011) and fast bilateral filtering (Paris & Durand, 2006; Tomasi & Manduchi, 1998; Chen et al., 2007). A common acceleration strategy applies the operator at low resolution and upsamples the result, but this results in blurry outputs. Bilateral space optimization (Barron et al., 2015; Barron & Poole, 2016) addresses this by solving an optimization problem within a bilateral grid. Similarly, (Chen et al., 2007) approximate an image operator using a grid of local affine models in bilateral space, where parameters are fit to a single input-output pair. (Gharbi et al., 2017) build upon this by training a neural network to apply the operator to unseen inputs. While most bilateral grid methods operate solely on single 2D images, our work extends this concept to the spatio-temporal domain, enabling multi-view consistent enhancement through a transformer-based architecture.

**Novel View Synthesis under Appearance Variations.** Extensions to NeRF (Mildenhall et al., 2020) and 3DGS (Kerbl et al., 2023) have attempted to solve novel view synthesis under real-world conditions such as inconsistent lighting, occlusions, and scene variability. The pioneering work NeRF-W (Martin-Brualla et al., 2021) incorporates per-image appearance and transient embeddings, with aleatoric uncertainty for transient object removal. Follow-ups improved NeRF robustness (Chen et al., 2021; Yang et al., 2023; Tancik et al., 2022), but suffer from slow optimization, rendering, and limited scalability. In low-light, RAW-NeRF (Mildenhall et al., 2021) leverages raw sensor data, but is constrained by long training times. For 3DGS, VastGaussian (Lin et al., 2024) applies CNNs to 3DGS outputs, but struggles with large appearance shifts. GS-W (Zhang et al., 2024) and WE-GS (Wang et al., 2024b) use CNN-derived reference features, while SWAG (Dahmani et al., 2024) and Scaffold-GS (Lu et al., 2024) store appearance data in a hash-grid-based implicit field (Müller et al., 2022). WildGaussians (Kulhanek et al., 2024) embeds appearance vectors within Gaussians, while Splatfacto-W (Xu et al., 2024) similarly combines Gaussian and image embeddings via an MLP to output spherical harmonics. Luminance-GS (Cui et al., 2025) predicts per-view color transforms followed by view-adaptive curve adjustment. DAVIGS (Lin et al., 2025) learns per-pixel affine transforms using an MLP combining per-view embeddings and 3D features. Most relevant to ours is BilaRF (Wang et al., 2024a), a NeRF-based method learning per-view bilateral grids to model camera ISP effects; recently extended to 3DGS (Xiao et al., 2025). However, all of these methods significantly increase training time. In contrast, we process the input images using a generalizable multi-view transformer, avoiding scene-specific optimization and preserving 3DGS efficiency.

## 3 METHODOLOGY

We propose a transformer model that takes as input a multi-view sequence of frames with varying appearances (e.g., exposure, white balance, color shifts) and predicts 3D bilateral grids to align each view with the reference frame. In this section, we first review bilateral grid processing (Sec. 3.1), then introduce our transformer architecture (Sec. 3.2) and reference frame selection mechanism (Sec. 3.3). We present our training strategy, leveraging self-supervision from a large feed-forward model, and detail our dataset construction process (Sec. 3.4). Our full pipeline overview is shown in Fig. 2.

### 3.1 PRELIMINARIES

**3D Bilateral Grids for Image Processing.** A 3D bilateral grid (Chen et al., 2007) is a compact data structure suitable for efficient modeling of spatially-varying edge-aware image transformations. It lifts image data into a lower resolution three-dimensional space defined by two spatial coordinates and a guidance dimension derived from the image intensity. By decoupling computational cost from image resolution and preserving semantic edges, bilateral grids enable real-time, and structure-aware processing, making them widely used for tone mapping, stylization, and artifact removal.

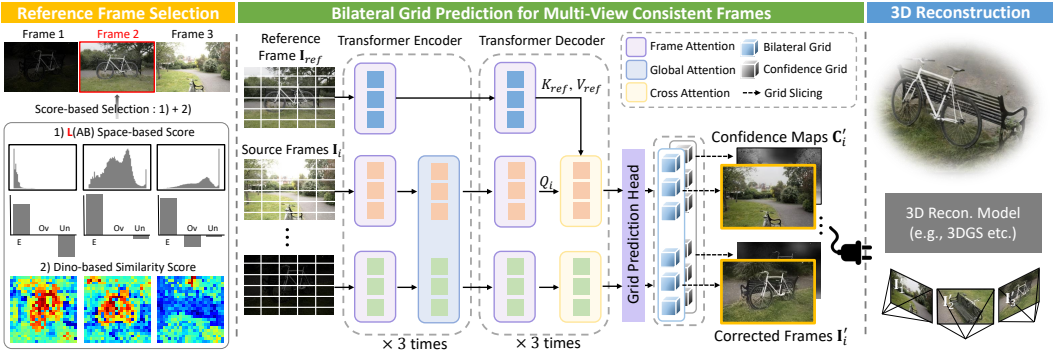


Figure 2: **Architecture Overview.** Our model first patchifies the reference frame  $\mathbf{I}_{ref}$  and  $N$  input multi-view source images  $\{\mathbf{I}_i\}_{i=1}^N$  into tokens. These are passed through the transformer encoder blocks comprising alternating frame-wise and global self-attention layers, repeated 3 times. The decoder uses alternating frame-attention and cross-attention with the reference frame. A final grid prediction head predicts the image and confidence bilateral grids ( $\mathbf{B}_i$  and  $\mathbf{C}_i$ ), which are subsequently *sliced* to produce the corrected frames  $\{\mathbf{I}'_i\}_{i=1}^N$  and confidence maps  $\{\mathbf{C}'_i\}_{i=1}^N$ . Based on our reference frame selection which chooses the frame with best photometric quality, we use the resulting harmonized images to train a wide range of 3D reconstruction models.

In the multi-view setting, we can model the appearance variations using per-view bilateral grids. We denote the  $i$ -th bilateral grid corresponding to the  $i$ -th image  $\mathbf{I}_i \in \mathbb{R}^{H \times W \times 3}$  as a tensor of local affine transformations  $\mathbf{B}_i \in \mathbb{R}^{H_s \times W_s \times D \times 12}$ , where  $H_s$ ,  $W_s$ , and  $D$  denote the spatial and guidance dimensions, respectively, such that  $(H_s, W_s) \ll (H, W)$ . The last dimension of size 12 corresponds to the flattened parameters of a  $3 \times 4$  affine transformation: a  $3 \times 3$  matrix  $\mathbf{A} \in \mathbb{R}^{3 \times 3}$  and a bias vector  $b \in \mathbb{R}^3$ . For input image  $\mathbf{I}$ , each pixel  $d$  with color  $I_d \in \mathbb{R}^3$  is transformed to its corresponding output pixel color  $I'_d \in \mathbb{R}^3$  by applying the affine transformation:  $I'_d = \mathbf{A}_d I_d + b_d$ , where  $\mathbf{A}_d$  and  $b_d$  are the affine parameters specific to pixel  $d$ . The parameters  $\theta_d = (\mathbf{A}_d, b_d)$  are obtained via trilinear interpolation over the neighboring vertices of the bilateral grid:

$$\theta_d = \sum_{i,j,k} w_{ijk}(d) \theta_{ijk}, \quad (1)$$

where  $\theta_{ijk} \in \mathbb{R}^{12}$  are the affine parameters at vertex  $(i, j, k)$ , and  $w_{ijk}(d)$  are interpolation weights determined by the spatial and guidance coordinates of pixel  $d$ . This process is known as *slicing*. For the guidance dimension, we use the pixel luminance following (Chen et al., 2007; Wang et al., 2024a). The bilateral grid resolution is much smaller than the input image resolution, reducing computational cost and preventing the bilateral grid from encoding the high-frequency content of the image.

### 3.2 MULTI-VIEW BILATERAL GRID TRANSFORMER

Our aim is to transform multi-view captures of a scene to be globally consistent, enabling robust 3D reconstruction and novel view synthesis under appearance variations. To achieve harmonization, we propose a multi-view aware transformer predicting per-patch bilateral grid parameters. This approach leverages the conceptual similarity between transformer patch-based processing and the structure of 3D bilateral grids where each vertex encodes a local affine color transformation. By predicting compact grid parameters per patch, which are applied to the original high-resolution images efficiently via lightweight slicing, our model learns spatially-varying image corrections that are consistent across views due to cross-frame attention, while balancing performance and computational cost.

**Model Processing and Outputs.** The input to our model is a sequence of  $N$  multi-view frames of a scene  $\{\mathbf{I}_i\}_{i=1}^N$  exhibiting potential appearance inconsistencies in color, exposure, white balance, etc. Here, a reference frame  $\mathbf{I}_{ref}$ , defining the target appearance, is selected via the protocol described in Sec. 3.3, while the remaining frames  $\mathbf{I}_{i \neq ref}^N$  serve as source images to be harmonized with  $\mathbf{I}_{ref}$ . First, each input image  $\mathbf{I}_i \in \mathbb{R}^{H \times W \times 3}$  is partitioned into non-overlapping patches  $\mathbf{P}_i \in \mathbb{R}^{H_P \times W_P \times J}$ , where the number of patches  $J$  is  $\frac{H}{H_P} \times \frac{W}{W_P}$ . Each patch  $\mathbf{P}_{i,j}$  is then projected into a feature vector by the patch encoder  $\Phi_{\text{embed}}$ . These feature vectors, combined with positional

---

encoding to retain the spatial information of each patch, form the input token sequence to our model:  $\mathbf{X} = \{\Phi_{\text{embed}}(\mathbf{P}_{i,j}) + \text{PE}_{i,j}\}_{i=1,j=1}^{N,J}$ . The input tokens are then processed with the main network  $f_\theta$ , yielding a set of 3D bilateral grids and confidence grids  $\{\mathbf{B}_i\}_{i \neq \text{ref}}^N \in \mathbb{R}^{H_s \times W_s \times D \times 12}$ , and  $\{\mathbf{C}_i\}_{i \neq \text{ref}}^N \in \mathbb{R}^{H_s \times W_s \times D \times 1}$ :

$$f_\theta(\mathbf{X}) = \{\mathbf{B}_i\}_{i \neq \text{ref}}^N, \{\mathbf{C}_i\}_{i \neq \text{ref}}^N, \quad (2)$$

where  $\{\mathbf{B}_i\}$  are applied to source frames  $\{\mathbf{I}_i\}_{i \neq \text{ref}}^N$  to get harmonized frames  $\{\mathbf{I}'_i\}$  via slicing (Sec. 3.1).

**Alternating Self and Cross Attention Architecture.** Fig. 2 shows our encoder-decoder transformer architecture, which adopts the alternating attention strategy of VGGT (Wang et al., 2025) to reduce memory cost while preserving the ability to model both intra- and cross-view interactions.

In the *encoder*, each block alternates between *local self-attention*, applied independently within each view to model spatial context and viewpoint-specific patterns, and *global self-attention*, which exchanges information across views at corresponding patch positions.

In the *decoder*, we explicitly align source frames  $\{\mathbf{I}_i\}_{i \neq \text{ref}}^N$  with the reference frame  $\mathbf{I}_{\text{ref}}$  to harmonize the appearance. Encoder outputs  $\{\mathbf{x}'_{i,j}\}_{i=1}^N$  are separated into  $\mathbf{x}'_{\text{ref},j}$  and  $\{\mathbf{x}'_{i,j}\}_{i \neq \text{ref}}^N$ , which are reference and source features, respectively. We replace global-attention layers with *cross-attention* between reference and sources tokens, enabling conditioning on the reference. Specifically, the key  $K$  and value  $V$  are extracted from  $\mathbf{x}'_{\text{ref},j}$ , while the query  $Q$  is extracted from  $\{\mathbf{x}'_{i,j}\}_{i \neq \text{ref}}^N$  for each decoder cross-attention block. With this framework, the refined features  $\{\mathbf{x}''_{i,j}\}_{i \neq \text{ref}}^N$  inherit consistent appearance guided by the reference feature  $\mathbf{x}'_{\text{ref},j}$ , yielding harmonized multi-view features.

**Bilateral Grid and Confidence Prediction Head.** The decoder’s output tokens for each source frame are used to predict the set of bilateral grids  $\{\mathbf{B}_i\}_{i \neq \text{ref}}^N$  to correct their appearance, rather than directly regressing corrected images. Each token  $\{\mathbf{x}''_{i,j}\}_{i \neq \text{ref}}^N$  predicts the per-intensity affine transformation parameters of the bilateral grids  $\{\mathbf{B}_{i,j}\} \in \mathbb{R}^{D \times 12}$ , where  $D$  is the intensity guidance dimension. Due to the conceptual similarity between the patch-based transformer model and bilateral grid, we can simply predict each grid-vertex parameters from each token using a small MLP. Per-pixel affine transforms obtained by slicing the resulting grids are applied to the source images obtaining the harmonized images  $\{\mathbf{I}'_i\}_{i \neq \text{ref}}^N$ .

In addition to bilateral grids, we make our model uncertainty-aware by predicting aleatoric uncertainty (Kendall & Cipolla, 2016); modeling inherent noise in the data, e.g., photometric variations in the ground truths or information loss in over-/under-exposed regions; thus stabilizing the training loss. Since we cannot directly obtain the confidence maps from our prediction head, as this would require a dense prediction head (Wang et al., 2025), we instead predict a low-resolution confidence grid along with each bilateral grid  $\{\mathbf{C}_i\} \in \mathbb{R}^{H_s \times W_s \times D \times 1}$ . Thus, for each patch position  $j$ , the grid prediction head outputs  $\{\mathbf{C}_{i,j}\} \in \mathbb{R}^{D \times 1}$ . Applying the slicing operation as before using the source images, we obtain full-resolution confidence maps  $\{\mathbf{C}'_{i,j}\} \in \mathbb{R}^{H \times W \times 1}$  that reflect the confidence of each pixel.

### 3.3 REFERENCE FRAME SELECTION

We employ a reference-frame-based strategy for two practical reasons: it maintains a consistent color space across frames, mitigating drift, and it allows explicit control over the final reconstruction appearance by specifying the reference frame. However, naively using the first or a random frame as the reference poses the risk of selecting an outlier, potentially causing drift or degrading quality, as shown in previous studies (Ren et al., 2020; Lee et al., 2022; Shin et al., 2025). To address this, we propose a method to select a reference frame that is both photometrically reliable and semantically representative at inference, as visualized in Fig. 2 (left).

We assess the semantic representativeness of each frame by computing cosine similarities of DINOv2 embeddings (Oquab et al., 2023). This yields a per-frame similarity score  $S_{\text{DINO}}$ , favoring those that contain rich scene information. However, as DINOv2 is robust to illumination variations, underexposed frames may also receive undesirably high similarity scores. Thus, we also assess the photometric quality of frames with respect to under-/over-exposure using the luminance channel  $L$  in CIE-LAB color space. We penalize frames with extreme over-/under-exposure ratios (e.g., below 5%

or above 95%) and combine this with the normalized entropy of the luminance distribution to form:

$$S_{\text{LAB}} = \lambda_{\text{ent}} \left( - \sum_l p(l) \log p(l) \right) + \lambda_{\text{ov}} \frac{1}{|L|} \sum_{i,j} [L_{ij} \geq 250] + \lambda_{\text{un}} \frac{1}{|L|} \sum_{i,j} [L_{ij} \leq 5], \quad (3)$$

where,  $p(l)$  is the probability of intensity level  $l$  estimated from the normalized luminance histogram, and  $\lambda_{\text{ent}}$ ,  $\lambda_{\text{ov}}$ , and  $\lambda_{\text{un}}$  are 1,  $-0.5$ , and  $-0.5$ , respectively. We define the overall score for frame  $i$  as  $S_i = \alpha \cdot S_{\text{LAB},i} + (1 - \alpha) \cdot S_{\text{DINO},i}$  and the frame with the highest  $S_i$  is chosen as the reference, where  $\alpha$  is set to 0.5. This pipeline maintains interpretability of reference-based harmonization while enabling automatic and robust selection.

### 3.4 TRAINING STRATEGY

**Training Objectives with Self-Supervised Guidance.** We train our model with the following probabilistic loss function (Kendall & Cipolla, 2016) to predict the corrected images:

$$\mathcal{L}_{\text{conf}} = \sum_{i=1}^N \mathbf{C}'_i \odot \|\hat{\mathbf{I}}_i - \mathbf{I}'_i\|_1 - \beta \log(\mathbf{C}'_i), \quad (4)$$

where  $\mathbf{I}'_i$  is the source image corrected with the bilateral grid  $\mathbf{B}_i$ . This probabilistic loss modulates the L1 loss between the corrected image  $\mathbf{I}'_i$  and the ground-truth image  $\hat{\mathbf{I}}_i$ , allowing the model to rely less on its predictions in challenging areas where image detail recovery is difficult. Along with  $\mathcal{L}_{\text{conf}}$ , we apply the total variation loss,  $\mathcal{L}_{\text{TV}}$ , encouraging smoothness of the bilateral grids:

$$\mathcal{L}_{\text{TV}} = \frac{1}{N} \sum_{i=1}^N \sum_{h,w,d} (\|\Delta_h \mathbf{B}_i(h, w, d)\|_2^2 + \|\Delta_w \mathbf{B}_i(h, w, d)\|_2^2 + \|\Delta_d \mathbf{B}_i(h, w, d)\|_2^2), \quad (5)$$

where  $\Delta$  denote forward difference operators.

As it is not straightforward to obtain real-world paired data to train our model, we further introduce a self-supervised loss. This enables training in cases without ground truth images and helps enforce view-consistency across frames. We leverage a large, pretrained feed-forward 3D reconstruction model  $h_\theta$  (e.g., AnySplat (Jiang et al., 2025)). Specifically, given a sequence of frames on each training iteration, we set the first frame as reference ( $\text{ref} = 0$ ) and predict camera poses  $\{p_i\}_{i=0}^N$  and Gaussian primitives  $\{\mathbf{G}_i\}_{i=0}^N$  from all the frames, including the first input frame  $\mathbf{I}_{\text{ref}}$  and the remaining corrected frames  $\{\mathbf{I}'_i\}_{i=1}^N$ . The predicted Gaussians for non-reference frames  $\{\mathbf{I}'_i\}_{i=1}^N$  are then reprojected to the viewpoint of the reference frame using predicted camera pose  $p_{\text{ref}}$ , and we compute the perceptual loss utilizing VGG features (Simonyan & Zisserman, 2014) between the original reference frame  $\mathbf{I}_{\text{ref}}$  and the rendered image. This encourages the outputs of our bilateral transformer network  $f_\theta$  to remain in a consistent color space, so that the downstream 3D reconstruction model  $h_\theta$  can build a coherent scene representation and generate stable novel views. Based on this, the self-supervised consistency loss  $\mathcal{L}_{ss}$  is defined as:

$$\mathcal{L}_{ss} = \text{VGG}(\mathbf{I}_{\text{ref}} - \text{Rasterizer}(p_{\text{ref}}, \{\mathbf{G}_i\}_{i=1}^N)), \quad \text{where} \quad \{p_i, \{\mathbf{G}_i\}_{i=0}^N\} = h_\theta(f_\theta(\{\mathbf{I}_i\}_{i=0}^N)), \quad (6)$$

with *Rasterizer* denoting the differentiable Gaussian rasterizer that projects the set of predicted Gaussian primitives  $\{\mathbf{G}_i\}$  into the viewpoint  $p_{\text{ref}}$  of the reference frame. Thus, our total loss is:

$$\mathcal{L} = \mathcal{L}_{\text{conf}} + \lambda_{\text{tv}} \mathcal{L}_{\text{TV}} + \lambda_{ss} \mathcal{L}_{ss}, \quad (7)$$

where  $\lambda_{\text{tv}}$  and  $\lambda_{ss}$  are set to 0.5 and 0.1, respectively.

**Training Datasets.** Acquiring large-scale multi-view paired data with realistic appearance variations is extremely challenging. Our approach handles this limitation by (i) simulating diverse and controllable variations in a synthetic setting, and (ii) introducing a self-supervised rendering loss that allows us to effectively learn from unpaired real-world data (Eq. 6). For paired data, we use

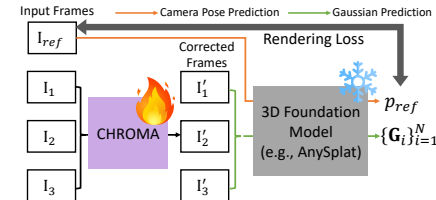


Figure 3: 3D Foundation Model based Self-Supervised Loss Pipeline.

multi-view consistent sequences from the DL3DV dataset (Ling et al., 2024) and synthesize realistic appearance variations by simulating camera ISP pipelines, thereby creating input–target pairs with controllable appearance changes. For unpaired data, we use the WildRGBD dataset (Xia et al., 2024), which captures objects under 360 degree rotations. As the viewpoint changes, the environmental lighting and camera’s auto-ISP settings induce appearance variations, such as fluctuating exposure, white balance and illumination, providing a realistic source of real-world inconsistencies. During training, the supervised loss  $\mathcal{L}_{conf}$  is applied only to paired data (DL3DV), while our self-supervised consistency loss  $\mathcal{L}_{ss}$  and total variation loss  $\mathcal{L}_{tv}$  are jointly optimized over both datasets. This enables our model to generalize well across both synthetic and real variations.

**Parametric Camera ISP Simulation.** We apply parametric camera ISP simulation on top of the DL3DV dataset (Ling et al., 2024). Building on the unprocessing framework of (Brooks et al., 2019), we reverse the camera pipeline to obtain linear RGB images and apply randomized variations in white balance, exposure, digital gain, gamma perturbation, and color correction matrices (CCMs). To realistically simulate illumination diversity, we model the exposure distribution as a bi-modal mixture representing both daytime and nighttime conditions. Specifically, exposure values  $e$  are drawn from:

$$e \sim \pi \mathcal{N}(\mu_{\text{day}}, \sigma_{\text{day}}^2) + (1 - \pi) \mathcal{N}(\mu_{\text{night}}, \sigma_{\text{night}}^2),$$

where  $(\mu_{\text{day}}, \sigma_{\text{day}})$  and  $(\mu_{\text{night}}, \sigma_{\text{night}})$  are the mean and variance of day and nighttime exposures respectively, and  $\pi \in [0, 1]$  controls the prior probability of day and night; set to (1.0, 0.2), (0.2, 0.1), 0.5, respectively. This simulates both well-lit and low-light scenes, enhancing robustness to ISP-induced inconsistencies under varying illumination conditions, as illustrated in Fig. 1(a).

**Implementation Details.** As Fig. 2 shows, our transformer encoder employs 3 layers of alternating frame-wise and global-attention. The decoder comprises 3 layers of alternating frame-wise and cross-attention. The model is relatively compact, with 137.84M parameters in total. We train by optimizing Eq. 7 with AdamW (Loshchilov & Hutter, 2017) for 70K iterations. We use dynamic batch loading to randomly sample between 4 and 24 frames from a selected multi-view scene (Sec. 3.4). Input images are resized to  $224 \times 224$  resolution with patch size  $8 \times 8$ , resulting in a total of  $28 \times 28 \times 8$  bilateral grid vertices per frame; one for each input image patch with a guidance dimension of  $D = 8$ . Training takes roughly a day with current GPU hardware (60 TFLOPS fp32 and 80 GB of memory).

## 4 EXPERIMENTS

We evaluate our method under three types of appearance variations: (a) *ISP variations*, (b) *exposure changes*, and (c) *real-world capture conditions*. This section describes the datasets used, baseline comparison methods, evaluation metrics, followed by detailed experimental results and ablations.

**Evaluation Datasets.** For (a) *ISP variations*, we use a camera ISP variation dataset derived from the DL3DV dataset (Ling et al., 2024). As described in Sec. 3.4, this includes white balance, exposure, gamma, and CCM adjustments. We evaluate on a diverse set of 25 held-out scenes which vary in content (indoor/outdoor), spatial characteristics (bounded/unbounded), and lighting conditions, as shown in the Appendix. For (b) *exposure variations*, we use the varying exposure LOM dataset released by Luminance-GS (Cui et al., 2025), which is based on the unbounded MipNeRF 360 dataset (Barron et al., 2022) with varying exposure and gamma correction. For (c) *real-captured scenes*, we evaluate on the real-world captured BilaRF dataset (Wang et al., 2024a), comprising mainly of nighttime scenes captured with flash illumination, posing real-world appearance shifts.

**Baselines.** We compare against state-of-the-art methods that incorporate appearance modeling into 3DGS: WildGaussians (Kulhanek et al., 2024), GS-W (Zhang et al., 2024), Luminance-GS (Cui et al., 2025), and 3DGS-4DBAG (Xiao et al., 2025) which jointly optimizes 3DGS and 4D bilateral grids. We also compare to vanilla 3DGS (Kerbl et al., 2023) (fast version from Taming-GS (Mallick et al., 2024)), 2DGS (Huang et al., 2024a), and DashGS (Chen et al., 2025).

**Metrics.** Quantitative evaluation is conducted using PSNR, SSIM, and LPIPS. When using appearance embeddings, the reconstructed color space may differ from the ground truth, leading to unfairly low scores despite accurate geometry. To address this, per-channel global affine color correction (CC) is applied to the rendered images, following (Wang et al., 2024a; Xiao et al., 2025; Mildenhall et al., 2021). Color-corrected metrics provide a more reliable measure of geometric quality under color discrepancies. Processing time on a mid-range GPU is also reported, including bilateral grid inference and reference frame selection on Ours.

Table 1: Comparison of our model combined with baseline 3D reconstruction methods, the baselines alone, and approaches using appearance embeddings. **CC** indicates per-channel affine color correction. Reported times include training; for our model, they also include processing overhead.

Dataset Method	PSNR $\uparrow$	PSNR CC $\uparrow$	SSIM $\uparrow$	SSIM CC $\uparrow$	LPIPS $\downarrow$	LPIPS CC $\downarrow$	Time (s) $\downarrow$
<i>DL3DV dataset w/ ISP variation</i>							
2DGS (Huang et al., 2024a)	22.78	26.81	0.8496	0.8608	0.2829	0.2169	13m 48s
3DGS (Kerbl et al., 2023)	21.43	26.25	0.8553	0.8749	0.2712	0.2069	3m 39s
DashGS (Chen et al., 2025)	23.35	28.17	0.8916	0.9029	0.2357	0.1782	3m 12s
WildGaussians (Kulhanek et al., 2024)	18.15	24.08	0.7663	0.8188	0.3050	0.2567	2h 10m 31s
GS-W (Zhang et al., 2024)	19.34	26.29	0.7910	0.8420	0.3092	0.2375	35m 54s
Luminance-GS (Cui et al., 2025)	20.00	26.14	0.7962	0.8466	0.2975	0.2290	14m 29s
<b>2DGS + Ours</b>	24.97	26.92	0.8564	0.8621	0.2312	0.2236	14m 3s
<b>3DGS + Ours</b>	<b>25.26</b>	<b>27.28</b>	<b>0.8650</b>	<b>0.8753</b>	<b>0.2191</b>	<b>0.2118</b>	3m 55s
<b>DashGS + Ours</b>	<b>26.45</b>	<b>28.92</b>	<b>0.8953</b>	<b>0.9035</b>	<b>0.1794</b>	<b>0.1703</b>	<b>3m 27s</b>
<i>LOM dataset w/ varying exposure</i>							
2DGS (Huang et al., 2024a)	16.75	22.03	0.5588	0.6724	0.3646	0.3622	25m 38s
3DGS (Kerbl et al., 2023)	16.50	21.00	0.5896	0.6715	0.3432	0.3517	4m 7s
DashGS (Chen et al., 2025)	17.01	21.94	0.6043	0.7052	0.3212	0.3221	3m 3s
WildGaussians (Kulhanek et al., 2024)	18.90	25.35	0.6470	0.7278	0.3261	0.3193	2h 30m 3s
GS-W (Zhang et al., 2024)	15.66	25.81	0.5256	0.7580	0.3385	0.2912	48m 45s
Luminance-GS (Cui et al., 2025)	18.12	23.12	0.6641	0.7352	0.3043	0.2851	22m 16s
<b>2DGS + Ours</b>	<b>18.99</b>	<b>26.37</b>	<b>0.7528</b>	<b>0.8125</b>	<b>0.2610</b>	<b>0.2446</b>	25m 50s
<b>3DGS + Ours</b>	<b>18.34</b>	<b>26.25</b>	<b>0.7554</b>	<b>0.8149</b>	<b>0.2592</b>	<b>0.2428</b>	<b>4m 19s</b>
<b>DashGS + Ours</b>	18.19	26.21	0.7507	0.8131	0.2610	0.2435	3m 14s
<i>BilaRF dataset</i>							
2DGS (Huang et al., 2024a)	-	23.43	-	0.746	-	0.308	13m 26s
3DGS (Kerbl et al., 2023)	-	24.23	-	0.8019	-	0.2594	3m 43s
DashGS (Chen et al., 2025)	-	24.34	-	0.7880	-	0.2607	3m 46s
WildGaussians (Kulhanek et al., 2024)	-	23.19	-	0.7424	-	0.3121	1h 58m 06s
GS-W (Zhang et al., 2024)	-	24.94	-	0.8056	-	0.2764	40m 34s
Luminance-GS (Cui et al., 2025)	-	23.41	-	0.7931	-	0.2750	18m 40s
2DGS-4DBAG (Xiao et al., 2025)	-	24.80	-	0.773	-	0.273	-
3DGS-4DBAG (Xiao et al., 2025)	-	24.90	-	0.774	-	0.256	-
<b>2DGS + Ours</b>	-	<b>25.27</b>	-	<b>0.8147</b>	-	<b>0.2499</b>	13m 30s
<b>3DGS + Ours</b>	-	<b>25.60</b>	-	<b>0.8240</b>	-	<b>0.2368</b>	<b>3m 48s</b>
<b>DashGS + Ours</b>	-	<b>26.25</b>	-	<b>0.8356</b>	-	<b>0.2158</b>	3m 50s

Table 2: Comparison with 2D image correction methods on the varying-exposure LOM dataset (Cui et al., 2025). Motion smoothness and temporal flickering from VBench (Huang et al., 2024b) are reported as the most relevant metrics for video quality under photometric correction.

Comparison with 2D Works	PSNR CC $\uparrow$	SSIM CC $\uparrow$	LPIPS CC $\downarrow$	motion smoothness $\uparrow$	temporal flickering $\uparrow$
CoTF (Li et al., 2024)	23.15	0.7573	0.2698	0.8591	0.8364
MSEC (Afifi et al., 2021)	23.98	0.7169	0.3359	0.8140	0.7848
MSLTNet (Zhou et al., 2024)	24.56	0.7697	0.2697	0.8248	0.7974
UEC (Cui et al., 2024)	<u>25.98</u>	<u>0.8143</u>	<b>0.2416</b>	0.8415	0.8124
<b>Ours</b>	<b>26.25</b>	<b>0.8149</b>	<u>0.2428</u>	<b>0.8707</b>	<b>0.8428</b>

#### 4.1 RESULTS

Table 1 reports quantitative results across all three datasets, with qualitative examples in Fig. 4. For all scenes, we employ our reference frame selection strategy (Sec. 3.3); no ground-truth image was used as reference for fair comparison. Despite the distinct characteristics of the three datasets, our method combined with 2DGS, 3DGS, or DashGS significantly outperforms each baseline, with fewer artifacts, and matches or surpasses per-scene appearance optimization methods. This demonstrates the robustness and generalizability of our model, and highlights the multi-view consistency leading to improved reconstructions. Moreover, methods with joint optimization of geometry and appearance introduce significant latency; more than doubling the overall training time. Notably, our model efficiently processes large-scale inputs, handling over 300 frames in a single forward pass. In practice, inference takes only about 2-3 seconds for BilaRF (roughly 30-70 images per scene), and up to 15 seconds for DL3DV and LOM, each containing more than 200 frames per scene.

Table 2 compares our method with 2D image exposure correction baselines prior to running 3DGS. Since these methods primarily target exposure adjustment, we conduct the comparison on the LOM dataset, containing mostly exposure-related variations. While these methods perform well on single frames, they lack multi-view consistency, resulting in degraded 3DGS performance. Similar to our method, UEC (Cui et al., 2024) uses an input reference exposure frame, but still operates

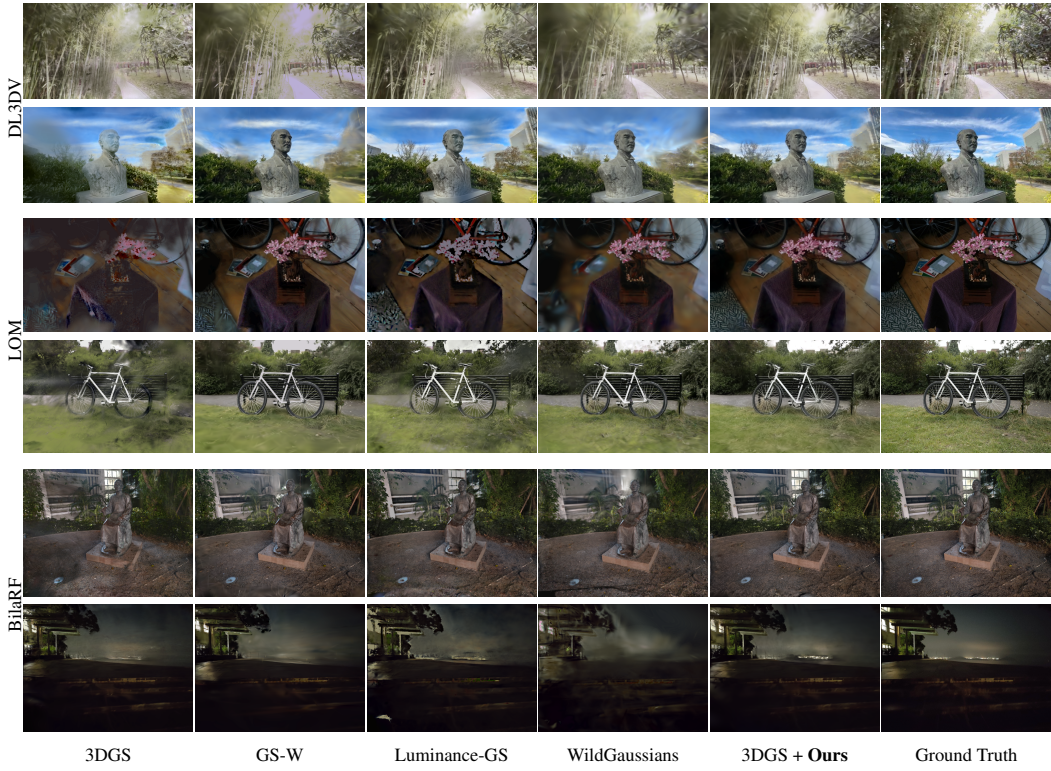


Figure 4: Qualitative results grouped by dataset: DL3DV, LOM, and BilaRF.

independently per frame, leading to lower overall performance. For fair comparison, we use the same reference frames for both our method and UEC, selected by our reference frame pipeline (Sec. 3.3).

Table 3: Ablation study. (Top) LOM dataset (Bottom) BilaRF dataset.

Ablation	PSNR CC	SSIM CC	LPIPS CC
single-frame processing	26.19	0.8131	0.2435
random reference frame	25.11	0.7559	0.3089
DINO-based reference frame	25.95	0.7871	0.2758
Ours (full)	<b>26.25</b>	<b>0.8149</b>	<b>0.2428</b>
w/o self-supervised loss	25.21	<b>0.8245</b>	0.2375
Ours (w/ self-supervised loss)	<b>25.60</b>	0.8240	<b>0.2368</b>

**Single-frame processing:** We observe that processing single-frame inputs independently yields slightly lower performance than processing the entire sequence in a single step, highlighting the importance of our transformer’s ability to leverage cross-view information. **Reference frame selection:** Simply choosing the first frame as the reference, which may be badly exposed or contain little semantic information (e.g. sky), significantly degrades performance. While DINO features help capture semantic similarity, the results show that relying on them alone is insufficient to robustly handle appearance variations, underscoring the importance of our dedicated reference frame selection mechanism.

**Self-supervised loss:** To assess the effect of the self-supervised consistency loss  $\mathcal{L}_{ss}$ , we evaluate on the held-out BilaRF dataset, which contains unpaired scenes with real-world variations. Incorporating  $\mathcal{L}_{ss}$  enables us to train on real-world unpaired data from the WildRGBD dataset. This helps bridge the domain gap from synthetic ISP variations (paired DL3DV data) to real-world appearance variations and yields clear gains in real-data performance.

We conduct ablations to isolate the contribution of each model component. Table 3 reports results on single vs multi-frame processing, reference frame selection, and the self-supervised loss. For experiments on multi-frame processing and reference frame selection, we use the LOM dataset, which exhibits large exposure variations across frames.

## 5 CONCLUSIONS

We have presented **CHROMA**, a feed-forward transformer framework for multi-view consistent harmonization via bilateral grid prediction. By explicitly enforcing photometric consistency across views, CHROMA integrates with existing 3D reconstruction pipelines without scene-specific optimization. Leveraging a large pretrained feed-forward model, we enable learning from unpaired data with self-supervision, improving robustness to real-world variations. Our reference frame selec-

---

tion strategy identifies a representative frame that is both photometrically and semantically reliable. Our experiments show that CHROMA consistently outperforms per-scene appearance embedding baselines, achieving higher reconstruction quality while reducing training overhead.

**Future Work.** Our model generalizes well to real-world appearance variations, and we plan to extend it to fully in-the-wild scenarios by modeling transient objects and integrating with larger feed-forward reconstruction frameworks (Wang et al., 2025; Jiang et al., 2025; Keetha et al., 2025). Unlike recent scene-specific in-the-wild methods (e.g., Kulhanek et al. (2024); Zhang et al. (2024); Wang et al. (2024b); Bai et al. (2025)), embedding our harmonization module into these models could enable a generalizable, feed-forward approach for 3D reconstruction from unconstrained photo collections.

---

## REFERENCES

Mahmoud Afifi and Michael S Brown. Deep white-balance editing. *CVPR*, 2020.

Mahmoud Afifi, Konstantinos G Derpanis, Bjorn Ommer, and Michael S Brown. Learning multi-scale photo exposure correction. *CVPR*, 2021.

Haiyang Bai, Jiaqi Zhu, Songru Jiang, Wei Huang, Tao Lu, Yuanqi Li, Jie Guo, Runze Fu, Yanwen Guo, and Lijun Chen. Gare: Relightable 3d gaussian splatting for outdoor scenes from unconstrained photo collections. *arXiv preprint arXiv:2507.20512*, 2025.

Jonathan T. Barron and Ben Poole. The fast bilateral solver. *ECCV*, 2016.

Jonathan T. Barron, Andrew Adams, Yichang Shih, and Carlos Hernández. Fast bilateral-space stereo for synthetic defocus. *CVPR*, 2015.

Jonathan T Barron, Ben Mildenhall, Dor Verbin, Pratul P Srinivasan, and Peter Hedman. Mip-nerf 360: Unbounded anti-aliased neural radiance fields. *CVPR*, 2022.

Tim Brooks, Ben Mildenhall, Tianfan Xue, Jiawen Chen, Dillon Sharlet, and Jonathan T Barron. Unprocessing images for learned raw denoising. *CVPR*, 2019.

Jiawen Chen, Sylvain Paris, and Frédéric Durand. Real-time edge-aware image processing with the bilateral grid. *ACM Transactions on Graphics (TOG)*, 2007.

Xingyu Chen, Qi Zhang, Xiaoyu Li, Yue Chen, Feng Ying, Xuan Wang, and Jue Wang. Hallucinated neural radiance fields in the wild. *CVPR*, 2021.

Youyu Chen, Junjun Jiang, Kui Jiang, Xiao Tang, Zhihao Li, Xianming Liu, and Yinyu Nie. Dash-gaussian: Optimizing 3d gaussian splatting in 200 seconds. *CVPR*, 2025.

Ruodai Cui, Li Niu, and Guosheng Hu. Unsupervised exposure correction. *ECCV*, 2024.

Ziteng Cui, Kunchang Li, Lin Gu, Shenghan Su, Peng Gao, ZhengKai Jiang, Yu Qiao, and Tatsuya Harada. You only need 90k parameters to adapt light: a light weight transformer for image enhancement and exposure correction. *BMVC*, 2022.

Ziteng Cui, Xuangeng Chu, and Tatsuya Harada. Luminance-gs: Adapting 3d gaussian splatting to challenging lighting conditions with view-adaptive curve adjustment. *CVPR*, 2025.

Hiba Dahmani, Moussab Bennehar, Nathan Piasco, Luis Roldão, and Dzmitry V. Tsishkou. Swag: Splatting in the wild images with appearance-conditioned gaussians. *ECCV*, 2024.

Zeev Farbman, Raanan Fattal, and Dani Lischinski. Convolution pyramids. *SIGGRAPH Asia*, 2011.

Michaël Gharbi, Jiawen Chen, Jonathan T Barron, Samuel W Hasinoff, and Frédéric Durand. Deep bilateral learning for real-time image enhancement. *ACM Transactions on Graphics (TOG)*, 2017.

Binbin Huang, Zehao Yu, Anpei Chen, Andreas Geiger, and Shenghua Gao. 2d gaussian splatting for geometrically accurate radiance fields. In *ACM SIGGRAPH 2024 conference papers*, pp. 1–11, 2024a.

Ziqi Huang, Yinan He, Jiashuo Yu, Fan Zhang, Chenyang Si, Yuming Jiang, Yuanhan Zhang, Tianxing Wu, Qingyang Jin, Nattapol Chanpaisit, et al. Vbench: Comprehensive benchmark suite for video generative models. In *Proceedings of the IEEE/CVF Conference on Computer Vision and Pattern Recognition*, pp. 21807–21818, 2024b.

Lihan Jiang, Yucheng Mao, Linning Xu, Tao Lu, Kerui Ren, Yichen Jin, Xudong Xu, Mulin Yu, Jiangmiao Pang, Feng Zhao, et al. Anysplat: Feed-forward 3d gaussian splatting from unconstrained views. *arXiv preprint arXiv:2505.23716*, 2025.

Nikhil Keetha, Norman Müller, Johannes Schönberger, Lorenzo Porzi, Yuchen Zhang, Tobias Fischer, Arno Knapitsch, Duncan Zauss, Ethan Weber, Nelson Antunes, et al. Mapanything: Universal feed-forward metric 3d reconstruction. *arXiv preprint arXiv:2509.13414*, 2025.

---

Alex Kendall and Roberto Cipolla. Modelling uncertainty in deep learning for camera relocalization. *ICRA*, 2016.

Bernhard Kerbl, Georgios Kopanas, Thomas Leimkühler, and George Drettakis. 3d gaussian splatting for real-time radiance field rendering. *ACM Transactions on Graphics (TOG)*, 2023.

Jonas Kulhanek, Songyou Peng, Zuzana Kukelova, Marc Pollefeys, and Torsten Sattler. Wildgaussians: 3d gaussian splatting in the wild. *NeurIPS*, 2024.

Youngjo Lee, Hongje Seong, and Euntai Kim. Iteratively selecting an easy reference frame makes unsupervised video object segmentation easier. In *Proceedings of the AAAI Conference on Artificial Intelligence*, pp. 1245–1253, 2022.

Ziwen Li, Feng Zhang, Meng Cao, Jinpu Zhang, Yuanjie Shao, Yuehuan Wang, and Nong Sang. Real-time exposure correction via collaborative transformations and adaptive sampling. *CVPR*, 2024.

Jiaqi Lin, Zhihao Li, Xiao Tang, Jianzhuang Liu, Shiyong Liu, Jiayue Liu, Yangdi Lu, Xiaofei Wu, Songcen Xu, Youliang Yan, et al. Vastgaussian: Vast 3d gaussians for large scene reconstruction. *CVPR*, 2024.

Jiaqi Lin, Zhihao Li, Bin Xiao Huang, Xiao Tang, Jianzhuang Liu, Shiyong Liu, Xiaofei Wu, Fenglong Song, and Wenming Yang. Decoupling appearance variations with 3d consistent features in gaussian splatting. *AAAI Conference on Artificial Intelligence*, 2025.

Lu Ling, Yichen Sheng, Zhi Tu, Wentian Zhao, Cheng Xin, Kun Wan, Lantao Yu, Qianyu Guo, Zixun Yu, Yawen Lu, et al. DL3dv-10k: A large-scale scene dataset for deep learning-based 3d vision. *CVPR*, 2024.

Ilya Loshchilov and Frank Hutter. Decoupled weight decay regularization. *ICLR*, 2017.

Tao Lu, Mulin Yu, Lining Xu, Yuanbo Xiangli, Limin Wang, Dahua Lin, and Bo Dai. Scaffold-gs: Structured 3d gaussians for view-adaptive rendering. *CVPR*, 2024.

Saswat Subhajyoti Mallick, Rahul Goel, Bernhard Kerbl, Markus Steinberger, Francisco Vicente Carrasco, and Fernando De La Torre. Taming 3dgs: High-quality radiance fields with limited resources. *SIGGRAPH Asia*, 2024.

Ricardo Martin-Brualla, Noha Radwan, Mehdi SM Sajjadi, Jonathan T Barron, Alexey Dosovitskiy, and Daniel Duckworth. Nerf in the wild: Neural radiance fields for unconstrained photo collections. *CVPR*, 2021.

Ben Mildenhall, Pratul P Srinivasan, Matthew Tancik, Jonathan T Barron, Ravi Ramamoorthi, and Ren Ng. Nerf: Representing scenes as neural radiance fields for view synthesis. *ECCV*, 2020.

Ben Mildenhall, Peter Hedman, Ricardo Martin-Brualla, Pratul P. Srinivasan, and Jonathan T. Barron. Nerf in the dark: High dynamic range view synthesis from noisy raw images. *CVPR*, 2021.

Thomas Müller, Alex Evans, Christoph Schied, and Alexander Keller. Instant neural graphics primitives with a multiresolution hash encoding. *ACM Transactions on Graphics (TOG)*, 2022.

Maxime Oquab, Timothée Darcet, Théo Moutakanni, Huy Vo, Marc Szafraniec, Vasil Khalidov, Pierre Fernandez, Daniel Haziza, Francisco Massa, Alaaeldin El-Nouby, et al. Dinov2: Learning robust visual features without supervision. *arXiv preprint arXiv:2304.07193*, 2023.

Sylvain Paris and Frédo Durand. A fast approximation of the bilateral filter using a signal processing approach. *IJCV*, 2006.

Jian Ren, Xiaohui Shen, Zhe Lin, and Radomir Mech. Best frame selection in a short video. In *Proceedings of the IEEE/CVF Winter Conference on applications of computer vision*, pp. 3212–3221, 2020.

Jisu Shin, Seunghyun Shin, and Hae-Gon Jeon. Task-specific scene structure representations. In *Proceedings of the AAAI Conference on Artificial Intelligence*, volume 37, pp. 2272–2281, 2023.

---

Jisu Shin, Junmyeong Lee, Seongmin Lee, Min-Gyu Park, Ju-Mi Kang, Ju Hong Yoon, and Hae-Gon Jeon. Canonicalfusion: Generating drivable 3d human avatars from multiple images. In *European Conference on Computer Vision*, pp. 38–56. Springer, 2024a.

Seunghyun Shin, Jisu Shin, Jihwan Bae, Inwook Shim, and Hae-Gon Jeon. Close imitation of expert retouching for black-and-white photography. *CVPR*, 2024b.

Seunghyun Shin, Dongmin Shin, Jisu Shin, Hae-Gon Jeon, and Joon-Young Lee. Video color grading via look-up table generation. *ICCV*, 2025.

Karen Simonyan and Andrew Zisserman. Very deep convolutional networks for large-scale image recognition. *arXiv preprint arXiv:1409.1556*, 2014.

Matthew Tancik, Vincent Casser, Xinchen Yan, Sabeek Pradhan, Ben Mildenhall, Pratul P. Srinivasan, Jonathan T. Barron, and Henrik Kretzschmar. Block-nerf: Scalable large scene neural view synthesis. *CVPR*, 2022.

Carlo Tomasi and Roberto Manduchi. Bilateral filtering for gray and color images. *ICCV*, 1998.

Jianyuan Wang, Minghao Chen, Nikita Karaev, Andrea Vedaldi, Christian Rupprecht, and David Novotny. Vggt: Visual geometry grounded transformer. *CVPR*, 2025.

Yuehao Wang, Chaoyi Wang, Bingchen Gong, and Tianfan Xue. Bilateral guided radiance field processing. *ACM Transactions on Graphics (TOG)*, 2024a.

Yuze Wang, Junyi Wang, and Yue Qi. We-gs: An in-the-wild efficient 3d gaussian representation for unconstrained photo collections. *ArXiv*, abs/2406.02407, 2024b.

Hongchi Xia, Yang Fu, Sifei Liu, and Xiaolong Wang. Rgbd objects in the wild: Scaling real-world 3d object learning from rgb-d videos. In *Proceedings of the IEEE/CVF Conference on Computer Vision and Pattern Recognition*, pp. 22378–22389, 2024.

Lu Xiao, Jiahao Wu, Zhanke Wang, Guanhua Wu, Runling Liu, Zhiyan Wang, and Ronggang Wang. Multi-view image enhancement inconsistency decoupling guided 3d gaussian splatting. In *ICASSP 2025-2025 IEEE International Conference on Acoustics, Speech and Signal Processing (ICASSP)*, pp. 1–5. IEEE, 2025.

Congrong Xu, Justin Kerr, and Angjoo Kanazawa. Splatfacto-w: A nerfstudio implementation of gaussian splatting for unconstrained photo collections. *ArXiv*, abs/2407.12306, 2024.

Yifan Yang, Shuhai Zhang, Zixiong Huang, Yubing Zhang, and Mingkui Tan. Cross-ray neural radiance fields for novel-view synthesis from unconstrained image collections. *ICCV*, 2023.

Dongbin Zhang, Chuming Wang, Weitao Wang, Peihao Li, Minghan Qin, and Haoqian Wang. Gaussian in the wild: 3d gaussian splatting for unconstrained image collections. *ECCV*, 2024.

Yijie Zhou, Chao Li, Jin Liang, Tianyi Xu, Xin Liu, and Jun Xu. 4k-resolution photo exposure correction at 125 fps with  $\sim 8$ k parameters. *WACV*, 2024.

Karel J. Zuiderveld. Contrast limited adaptive histogram equalization. In *Graphics Gems*, 1994.